Steel and Composite Structures, *Vol. 22, No. 2 (2016) 449-472*
DOI: http://dx.doi.org/10.12989/scs.2016.22.2.449

Seismic behavior of composite walls with encased steel truss

Yun-tian Wu [*1,2], Dao-yang Kang [2a], Yi-ting Su [2b] and Yeong-bin Yang [2c]

[1] *Key Laboratory of New Technology for Construction of Cities in Mountain Area, Ministry of Education, China*
[2] *School of Civil Engineering, Chongqing University, Chongqing 400045, China*

(*Received December 17, 2015, Revised September 28, 2016, Accepted October 13, 2016*)

Abstract. This paper studies the seismic behavior of reinforced concrete (RC) walls with encased cold-formed and thin-walled (CFTW) steel truss, which can be used as an alternative to the conventional RC walls or steel reinforced concrete (SRC) composite walls for high-rise buildings in high seismic regions. Seven one-fourth scaled RC wall specimens with encased CFTW steel truss were designed, manufactured and tested to failure under reversed cyclic lateral load and constant axial load. The test parameters were the axial load ratio, configuration and volumetric steel ratio of encased web brace. The behaviors of the test specimens, including damage formation, failure mode, hysteretic curves, stiffness degradation, ductility and energy dissipation, were examined. Test results indicate that the encased web braces can effectively improve the ductility and energy dissipation capacity of RC walls. The steel angles are more suitable to be used as the web brace than the latticed batten plates in enhancing the ductility and energy dissipation. Higher axial load ratio is beneficial to lateral load capacity, but can result in reduced ductility and energy dissipation capacity. A volumetric ratio about 0.25% of encased web brace is believed cost-effective in ensuring satisfactory seismic performance of RC walls. The axial load ratio should not exceed the maximum level, about 0.20 for the nominal value or about 0.50 for the design value. Numerical analyses were performed to predict the backbone curves of the specimens and calculation formula from the Chinese Code for Design of Composite Structures was used to predict the maximum lateral load capacity. The comparison shows good agreement between the test and predicted results.

Keywords: wall; seismic performance; axial load ratio; brace; high-rise building

1. Introduction

Reinforced concrete (RC) structural walls have been widely used in high-rise buildings located in seismic regions for high lateral strength and stiffness required for the resistance of wind and earthquake ground motion. Previous experimental studies (e.g., Vallenas *et al*. 1979, Hines *et al*. 2002, Sayre 2003, Thomsen and Wallace 2004, Dazio *et al*. 2009) have revealed that in spite of the complex response characteristics of RC walls under earthquake ground motions largely due to the nonlinear shear-flexure interaction and the axial load-flexure interaction, RC walls can be designed and detailed to have sufficient load carrying capacity, deformation and energy dissipation

*Corresponding author, Associate Professor, E-mail: yuntianw@cqu.edu.cn
[a] Research Assistant
[b] Research Assistant
[c] Professor

 ISSN: 1229-9367 (Print), 1598-6233 (Online)

capacities with acceptable cost-effectiveness. However, circumstances do occur when the conventional RC walls are not adequate for the seismic resistance. Firstly, in super high-rise buildings exceeding the height limits specified in building codes, the lower stories and basements are subjected to tremendously large axial loads, which will significantly reduce the load carrying capacity and ductility performance of RC walls, unless unreasonably large wall thickness is provided. By adding steel shapes, the axial load carrying capacity and lateral force resisting mechanism of RC walls can be improved without much increase in wall thickness, resulting in the so-called steel reinforced concrete (SRC) composite walls, as shown in Fig. 1. Different types of SRC composite walls have been studied and widely used in seismic zones in order to obtain adequate vertical and lateral load carrying capacity, ductility, post-yielding behavior and energy dissipation capacity (Zhao and Astaneh-Asl 2004, Cao *et al*. 2009, Eom *et al*. 2009, Dan *et al*. 2011, Nie *et al*. 2013 and Rafiei *et al* 2015). Secondly, for ordinary high-rise buildings located in high seismic regions (e.g., design peak ground acceleration up to 0.4 g), although conventional RC walls can be used since the building heights are below the code specified limits, excessive amount of longitudinal and transverse reinforcing bars have to be provided to ensure the structural safety, causing extreme difficulties in construction and extra cost for quality control due to the reinforcement congestion problem. The SRC composite walls may not be a good choice due to its high cost. Thus cost-effective solutions for such high-rise buildings located in high seismic regions should be further developed.

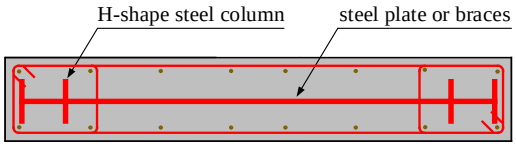

Fig. 1 Typical steel reinforced concrete composite wall

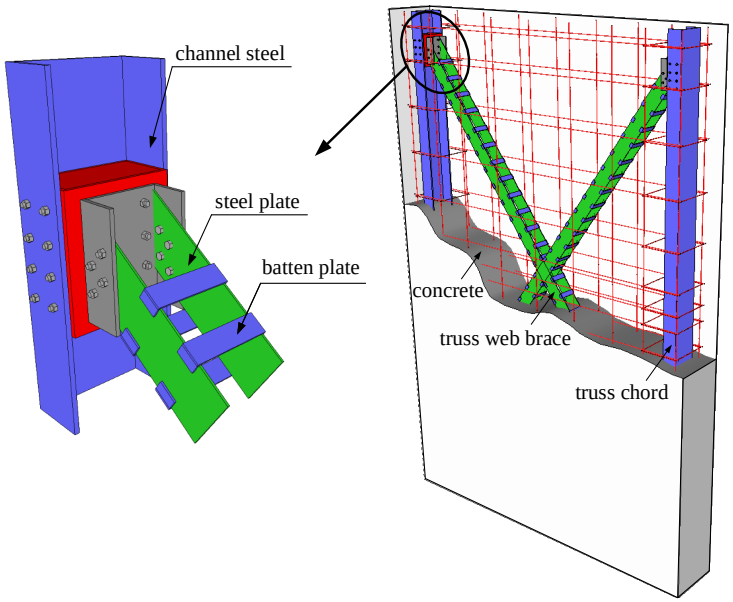

Fig. 2 Proposed details for composite walls with encased CFTW steel truss

In this study, a novel type of composite structural wall, as shown in Fig. 2, where cold-formed and thin-walled (CFTW) steel shape comparable to equivalent reinforcing bars in amount is encased in RC walls in the form of truss, is proposed to provide a cost-effective solution to ensure the constructability as well as seismic performance of ordinary high-rise buildings located in high seismic regions. Considering the parameters of axial load ratio, volumetric ratio of the encased truss web braces, and the form of web brace, a series of experiments were conducted to investigate the seismic behavior of RC wall specimens with encased CFTW steel truss in terms of strength, stiffness, ductility and energy dissipation capacity under constant axial load and reversed cyclic loading. Then reliable numerical finite element analyses were performed to obtain the backbone curves of the specimens to verify the main test results. Calculation formula from the Chinese Code for Design of Composite Structures (JGJ138-2012 2012) was used to predict the maximum lateral load capacity. Design suggestions are also given based on the experimental results.

2. Experimental program

2.1 Details of specimens

The test specimens were designed to simulate the structural walls for ordinary high-rise buildings in high seismic regions, and were fabricated at an approximate 1/4 scale to accommodate the capacity of the loading facility. Seven specimens labeled by CTSRC-1 to CTSRC-7 were constructed and tested subjected to constant axial load and cyclic reversed lateral loading. The primary parameters were the axial load ratio, configuration and volumetric steel ratio of encased web brace. All the specimens had the same overall geometrical dimensions, consisting of a 900 mm × 300 mm × 300 mm loading block on top, a 800 mm × 120 mm × 1290 mm wall portion and a 1500 mm × 350 mm × 450 mm base block at bottom. The aspect ratio of wall height l_w to width of wall cross section h_w of each specimen was around 1.8, indicating that the shear-flexure behavior interaction would dominate the overall behavior. The specimens were designed based on the Chinese Code for Seismic Design of Buildings (GB50011-2010 2010). No. 6 (6 mm nominal diameter) hot-rolled ribbed bars (HRB) were used as the vertical and horizontal web reinforcements spaced by 120 and 100 mm respectively. Six No. 8 HRBs were placed as the longitudinal reinforcement at the boundary elements in all specimens. Fig. 3 shows the dimensions and details of the seven specimens, including the cross sectional dimensions of encased steel truss. All specimens contained vertical channel steel shape C60×30×2.5 at the boundary elements, resulting in a 0.625% of steel ratio, defined as the ratio of cross sectional area of channel steel shape to the total wall cross sectional area. The encased web brace member was steel angles ∟30×30×2 in specimens CTSRC-1, CTSRC-5 and CTSRC-6 and that in CTSRC-7 was ∟50×30×3. Latticed batten plates with cross sectional dimensions of 60 mm × 1 mm and 80 mm × 1.5 mm were used as encased web brace in specimens CTSRC-3 and CTSRC-4 respectively. The parameters of all specimens are summarized in Table 1, where the axial load ratio α is defined as the ratio of applied axial load to the total axial load carrying capacity of wall cross section and the volumetric steel ratio of encased truss web brace, ρ_{vb} is defined as the ratio of the volume of web braces to that of the entire wall. The axial load ratios were 0.10 for specimens CTSRC-1 to CTSRC-4, 0.20 for specimen CTSRC-5 and 0.25 for specimens CTSRC-6 to CTSRC-7, respectively. The volumetric steel ratios of encased web braces were 0.25% for specimens CTSRC-2, CTSRC-3, CTSRC-5 and CTSRC-6, 0.50% for specimens CTSRC-4 and CTSRC-7. Web braces were not used in specimens CTSRC-1 for the purpose of comparison. The influences

Table 1 Parameters of specimens

Specimen	Applied axial load (kN)	Axial load ratio, α	Web brace member	Volumetric ratio of web brace, ρ_{vb} (%)	Steel ratio of steel truss chord, ρ_c (%)	φ
CTSRC-1	522	0.10	None	0	0.625	0
CTSRC-2	512	0.10	∟30×30×2	0.25	0.625	0.536
CTSRC-3	524	0.10	—60×1	0.25	0.625	0.922
CTSRC-4	547	0.10	—80×1.5	0.50	0.625	0.922
CTSRC-5	1187	0.20	∟30×30×2	0.25	0.625	0.536
CTSRC-6	1315	0.25	∟30×30×2	0.25	0.625	0.536
CTSRC-7	1315	0.25	∟50×30×3	0.50	0.625	0.517

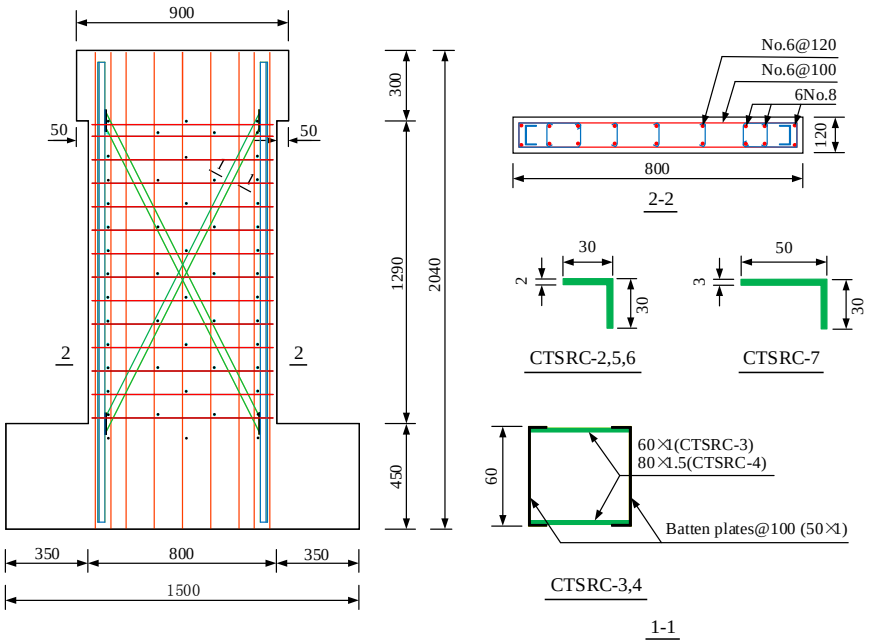

Fig. 3 Details of specimens (all dimensions are in mm)

of α and ρ_{vb} on the overall behavior of RC walls with encased CFTW steel truss can be evaluated by the comparison of test results of specimens.

2.2 Test setup and loading procedure

The test specimen was placed in a loading frame in the structural laboratory of Chongqing University, as shown in Fig. 4. The base block was fastened to the strong floor by a pair of rigid beams with high strength steel rods to prevent the overturning. Two jacks were also placed against the front and rear surfaces of the base block of each specimen to avoid horizontal sliding. The loading block was connected to a vertical hydraulic jack with a maximum loading capacity of 1500 kN for the application of axial load, and to a horizontal servo-controlled actuator with a maximum

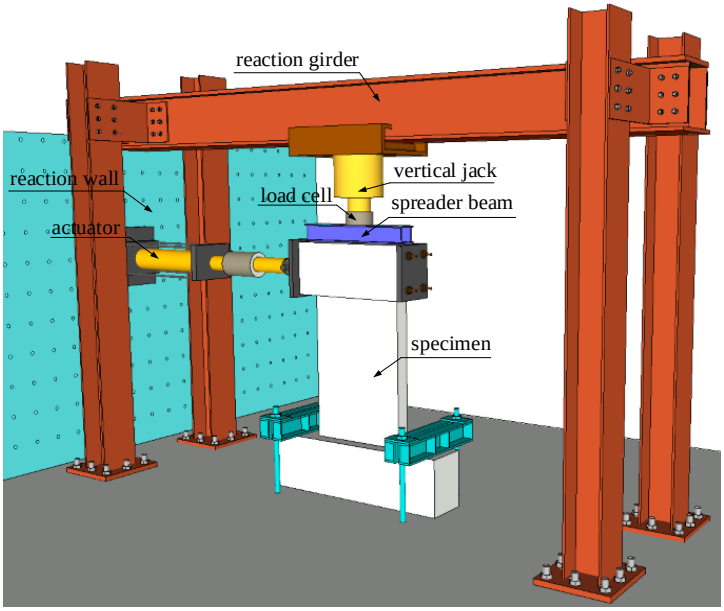

Fig. 4 Test setup

loading capacity of 1000 kN and a stroke of ± 100 mm. The axial load was applied to the specimen prior to the commencement of horizontal loading. A spreader beam was placed between the vertical jack and the top surface of the specimen so as to distribute the axial load uniformly across the entire wall cross section. A high precision load cell was mounted on the jack to monitor and approximately maintain constantly the applied axial load during testing. For convenience the pushing and pulling of the horizontal actuator were regarded as the positive and negative loading directions respectively.

The lateral cyclic loading procedure was divided into load-controlled and displacement-controlled stages. The load-controlled stage started from loading in the positive direction with an increment of 20 kN. When the lateral load was 80 kN, the load increment was reduced to 10 kN until the initial cracking was observed. Then similar loading pattern was applied in the negative loading direction until the cracking load was found. The subsequent loading cycles were displacement controlled till the termination of test. Before the specimen yielded, the lateral displacement increment was 3 mm. Then the displacement increment became 4 mm till the test was terminated. Two cycles of loading were repeated corresponding to each displacement level until the strength of the specimens decreased to 85% of the maximum lateral load.

2.3 Instrumentation

Strains and displacements at critical locations were measured for each specimen, as shown in Fig. 5(a). Five displacement transducers were mounted against a rigid steel reference frame to measure the lateral displacements at 300 mm intervals over the wall height. Two pairs of diagonally arranged displacement transducers were used to measure the shear deformation of the specimens. Six linear variable differential transducers (LVDTs) with a stroke of ± 100 mm were mounted vertically along the length of each wall so that the deformation of the wall base could be

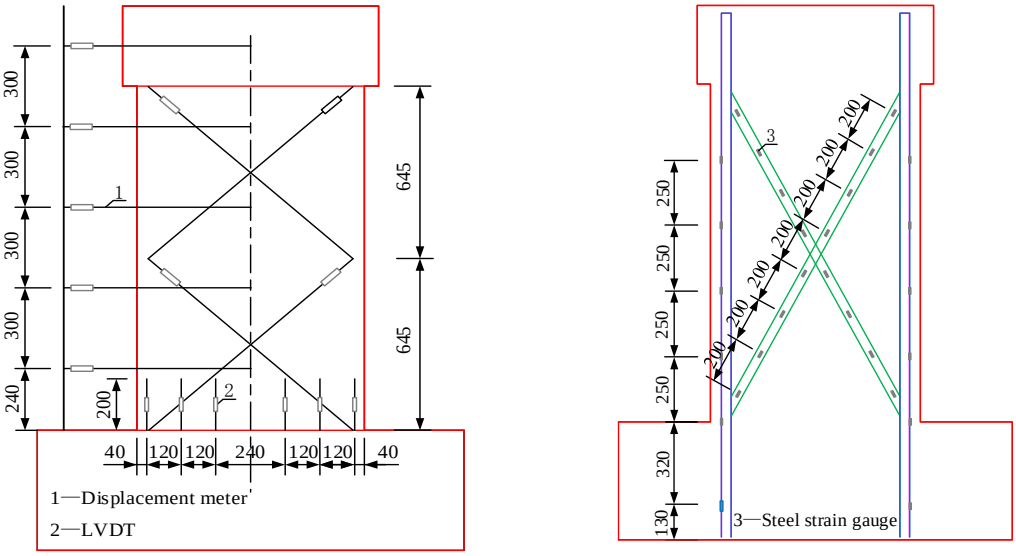

(a) Displacement transducers and LVDTs (b) Strain gauge arrangement

Fig. 5 Instrumentation plan (all dimensions are in mm)

determined. The strains of the vertical boundary and vertical web reinforcing bars were measured by strain gauges. The strains of the steel were measured as well, as illustrated in Fig. 5(b). The measurement was recorded by a computer data acquisition system. In addition, the cracking of wall was monitored to observe the damage development process of the specimens.

2.4 Material properties

The concrete used for the specimens had a strength grade of C60, for which the nominal cubic compressive strength is 60 MPa. The actual average compressive strength of the wall concrete were 59.2 MPa, 58.7 MPa, 59.5 MPa, 62.4 MPa, 59.3 MPa, 60.1 MPa and 59.2 MPa respectively measured on the days of testing. Tensile tests on steel coupons were also done to determine the yield strength (f_y) and tensile strength (f_t) of steel material. The experimental results related to the main mechanical properties of reinforcing bars, encased steel are listed in Table 2.

Table 2 Steel material properties

Steel type	Yield stress f_y (N/mm^2)	Ultimate stress f_t (N/mm^2)	Elastic stress E_s (N/mm^2)	Yield strain ε_y
C60×30×2.5	384.2	414.1	2.13×10^5	1.808×10^{-3}
∟30×30×2	344.2	409.8	2.06×10^5	1.892×10^{-3}
∟50×30×3	365.5	425.5	2.05×10^5	1.786×10^{-3}
—60×1	307.0	395.7	1.94×10^5	1.579×10^{-3}
—80×1.5	329.5	369.5	1.94×10^5	1.699×10^{-3}
No. 6 HRB	358.3	512.3	2.21×10^5	1.620×10^{-3}
No. 8 HRB	362.5	520.4	2.37×10^5	1.529×10^{-3}

3. Numerical finite element prediction

Prior to conducting the experimental tests, numerical finite element models were developed using the proved-reliable finite element analysis program (DIANA Version 9.4.4 2012) and simulations performed to predict the main experimental results.

3.1 Concrete

In the finite element analysis, three dimensional solid elements named CHX60 were used to discretize the wall concrete. The total strain rotating crack model was adopted to simulate the cracking characteristics of concrete. According to this model, when the principle tensile stress exceeds the specified limit, cracks appear in the perpendicular direction. The compressive stress-strain relationship of concrete used in the analysis is illustrated in Fig. 6. The parabolic compressive stress-strain relationship of concrete is defined by

$$\sigma = \begin{cases} -f_c \dfrac{\varepsilon_j}{3\varepsilon_{c/3}} & \varepsilon_{c/3} < \varepsilon_j \le 0 \\ -f_c \dfrac{1}{3}\left(1+4\left(\dfrac{\varepsilon_j-\varepsilon_{c/3}}{\varepsilon_c-\varepsilon_{c/3}}\right)-2\left(\dfrac{\varepsilon_j-\varepsilon_{c/3}}{\varepsilon_c-\varepsilon_{c/3}}\right)^2\right) & \varepsilon_c < \varepsilon_j \le \varepsilon_{c/3} \\ -f_c\left(1-\left(\dfrac{\varepsilon_j-\varepsilon_c}{\varepsilon_u-\varepsilon_c}\right)^2\right) & \varepsilon_u < \varepsilon_j \le \varepsilon_c \end{cases} \tag{1}$$

where f_c is the compressive strength of concrete; $\varepsilon_{c/3}$, ε_c and ε_u are the concrete strains corresponding to 1/3 f_c, f_c and ultimate condition, and can be expressed by Eqs. (2)-(4) respectively

$$\varepsilon_{c/3} = -\frac{f_c}{3E} \tag{2}$$

$$\varepsilon_c = -\frac{5f_c}{3E} = 5\varepsilon_{c/3} \tag{3}$$

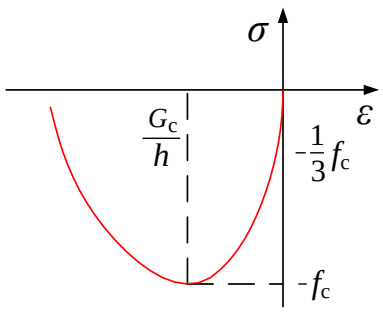

Fig. 6 Compressive stress-strain curve of concrete

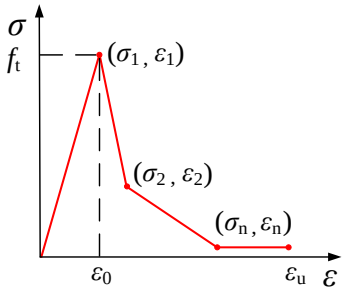

Fig. 7 Tensile stress-strain curve of concrete

$$\varepsilon_u = \varepsilon_c - \frac{3G_C}{2hf_c} \tag{4}$$

where E is the Young's modulus; G_C is the total compressive fracture energy of concrete ranging from 10 to 25 N-mm/mm^2 according to Feenstra (1993).

The tensile stress-strain relationship of concrete used in the analysis is depicted in Fig. 7. The tensile strength of concrete f_t was determined in accordance with the Chinese Code for Design of Concrete Structures (GB50010-2010 2010). ε_0 and ε_u are the tensile strains corresponding to f_t and the ultimate condition, which were taken as 0.000118 and 0.0014 respectively.

3.2 Reinforcement and steel

The modeling of reinforcing bars and encased CFTW steel truss was treated differently in order to balance the simulation accuracy and computational cost. The reinforcing bars were considered using encased reinforcement model, where the reinforcement element is encased in the concrete element so that the strain of the reinforcement is compatible with that of concrete element. The flat shell element named CQ40F, on the other hand, was used to model the encased CFTW truss chord and web braces. The tri-linear stress-strain model, as shown in Fig. 8, was used for simulating the reinforcing bars and the shaped steel.

3.3 Meshing of finite element models of test specimens

The meshing of the finite element models is important to the analysis. Although a more refined

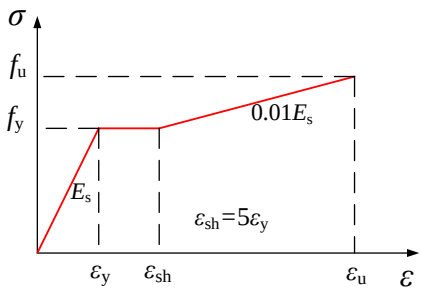

Fig. 8 Stress-strain relationship of steel

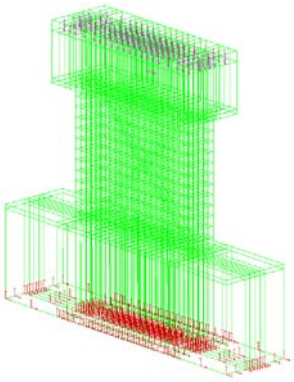

Fig. 9 Typical DIANA model of specimens

meshing can generally result in analysis results with better accuracy, the computational cost will be largely increased or even cause difficulty in convergence. In the present study, the walls with 1290mm height and 650mm width were equally divided into 16 and 30 segments, respectively. And the thickness of walls was equally divided into two segments. Although the element size can be further reduced to obtain a more refined meshing scheme, no obvious difference in calculation results was observed. A typical DIANA model of the test specimens is shown in Fig. 9.

3.4 Solution algorithm

The Regular Newton-Raphson method was adopted for the solution algorithm of the nonlinear functions. Compared with the Modified Newton-Raphson method, more precise results can be calculated by the regular Newton-Raphson method. The energy convergence standard was adopted to determine if the iteration was converged or not. The convergence toleration was 0.001 after the maximum iteration number of 30 times.

4. Prediction based on Chinese design code JGJ138-2012 (2012)

The load carrying capacity of RC walls with encased CFTW steel truss can also be evaluated by the Chinese Code for Design of Composite Structures (JGJ138-2012 2012)

$$V_u^c = \frac{1}{\lambda - 0.5}\left(0.5 f_t b_w h_{wo} + 0.13N\frac{A_w}{A}\right) + f_{yv}\frac{A_{sh}}{s}h_{w0} + \frac{0.3}{\lambda} f_a A_a + \left(f_g A_g + \varphi f_g^{'} A_g^{'}\right)\cos\alpha \qquad (5)$$

where λ is the shear span ratio of the wall section subjected to bending moment M and shear force V, which can be calculated by

$$\lambda = \begin{cases} 1.5 & M/Vh_{w0} < 1.5 \\ M/Vh_{w0} & 1.5 \le M/Vh_{w0} \le 2.2 \\ 2.2 & M/Vh_{w0} > 2.2 \end{cases} \qquad (6)$$

f_c is the compressive strength of concrete; b_w is the thickness of structural wall; h_{w0} is the

effective depth of wall section measured from extreme compression fiber to centroid of longitudinal reinforcing bars and steel chord member at the boundary element in tension; N is the axial load; A_w is the web area of wall; A is the total cross sectional area of wall; f_{yv} is the tensile strength of horizontal distributed reinforcement; s is the vertical spacing of horizontal distributed reinforcement; A_{sh} is the total area of the horizontal distributed reinforcement; f_a is the tensile strength of shape steel at the boundary of wall; A_a is the area of shape steel on the tension side of wall; f_g nd f'_g are the tensile and compressive strength of shape steel diagonal bracing member; A_g and A'_g are the tensile and compressive areas of shape steel diagonal bracing; φ is the stability coefficient of the web brace in compression according to the Chinese code for design of steel structures (GB500017-2003 2003), and the value for each specimen is shown in Table 1; α is the angle between the web brace and horizontal plane, which is about sixty degrees for all the test specimens.

5. Results and discussion

5.1 Cracking and damage patterns

Fig. 10 shows the cracking process of the specimen CTSRC-2 corresponding to initial cracking, horizontal crack extending, inclined crack forming and concrete spalling respectively. The first horizontal crack (Fig. 10(a)) appeared when the horizontal load was 100 kN and was 130 mm away from the bottom section of wall. New horizontal cracks were developed and further extended towards the web region of the wall upon further loading (Fig. 10(b)), indicating that the specimen was mainly subjected to bending moment in the early loading stage. As the lateral displacement was increased, more inclined cracks came into being along the height of the wall boundaries,

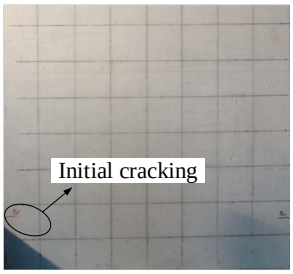

(a) Initial crack

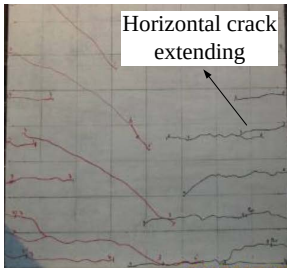

(b) Horizontal crack extending

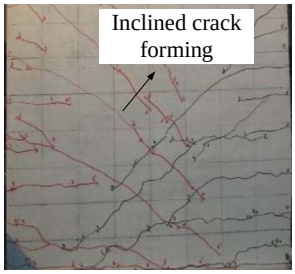

(c) Inclined cracks forming

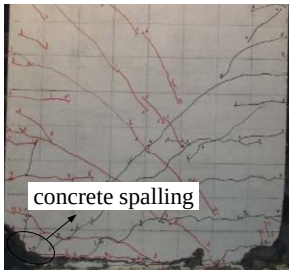

(d) Concrete spalling

(e) wall base corner at failure

Fig. 10 Failure mode of specimen CTSRC-2

and propagated toward the bottom region with angles of roughly 40 degrees (Fig. 10(c)). Yielding of the outermost vertical boundary element reinforcement on the tension side was observed corresponding to the lateral displacement of 6.0 mm. At the lateral displacement of 9.0 mm, the specimen attained its maximum lateral load capacity P_m. After the lateral load started to decrease, major diagonal cracks continuously developed until the entire surface of the wall was separated by intercrossing inclined cracks. The development of diagonal cracks suggested an increasing impact of shear forces on the damage of specimen during the loading process. The chord member of the encased truss on the tension side of the wall started to yield during the first cycle of the positive loading at the lateral displacement of 12 mm. Finally, spalling of concrete at the extreme compression fibers near the base of the wall was observed (Fig. 10(d)). The ultimate condition of the wall corner is shown in Fig. 10(e). The distributed reinforcements were exposed and buckled.

The specimens CTSRC-2, CTSRC-5 and CTSRC-6 had the same volumetric steel ratio and web brace configuration while different axial load ratios. As shown in Fig. 11, corresponding to the smallest axial load ratio (Fig. 11(a)), the largest number of short length horizontal cracks along the height of boundary elements was developed in CTSRC-2 among these three specimens. Specimens CTSRC-5 (Fig. 11(b)) and CTSRC-6 (Fig. 11(c)), with higher levels of axial load than CTSRC-2, exhibited much more severe damage at bottom regions of both boundary elements and web.

As shown in Fig. 12, the cracking and failure pattern of specimens CTSRC-1 (Fig. 12(a)), CTSRC -3 (Fig. 12(b)) and CTSRC-4 (Fig. 12(c)) were similar to CTSRC-2, with the same axial load ratio of 0.10. The web braces of specimens CTSRC-3 and CTSRC-4 were latticed batten plates instead of the steel angles in CTSRC-2, indicating that under a low level of axial load ratio, the volumetric steel ratio and the web brace configuration had little influence on the damage process of specimens.

The axial load ratio was 0.25 for specimens CTSRC-6 (Fig. 13(a)) and CTSRC-7 (Fig. 13(b)). The volumetric steel ratio of web brace of CTSRC-7 was 0.50%, higher than that of CTSRC-6. Though the ultimate concrete spalling conditions at bottom regions of the boundary elements were similar, the inclined cracks on the surface of CTSRC-7 had shorter length and were more uniformly distributed than CTSRC-6, as shown in Fig. 13.

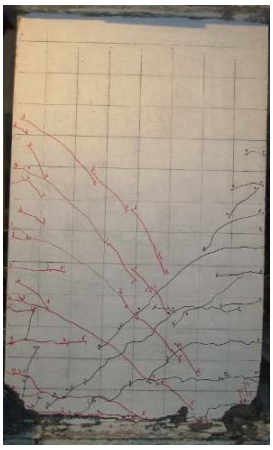

(a) CTSRC-2, α = 0.10

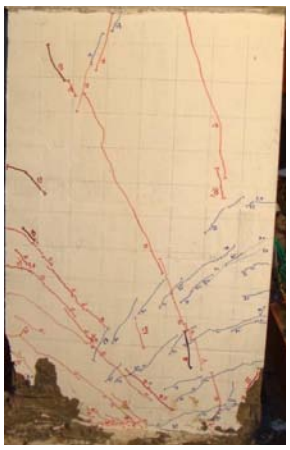

(b) CTSRC-5, α = 0.20

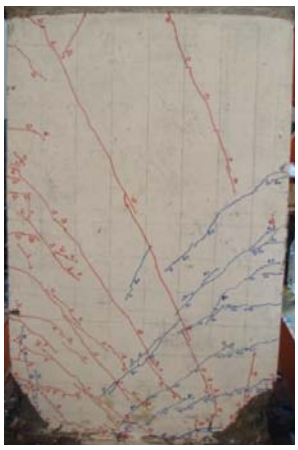

(c) CTSRC-6, α = 0.25

Fig. 11 Influence of axial load ratio

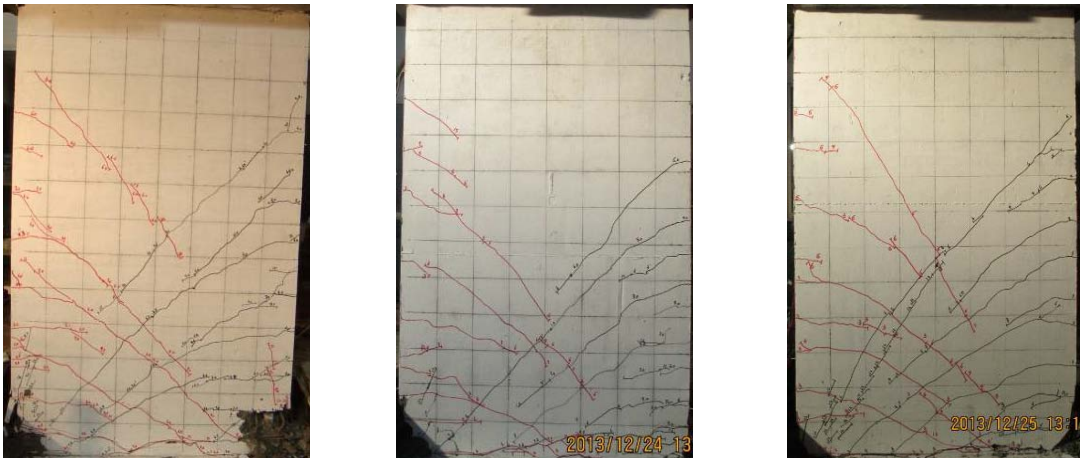

(a) CTSRC-1, ρ_{vb} = 0 (b) CTSRC-3, ρ_{vb} = 0.25% (c) CTSRC-4, ρ_{vb} = 0.50%

Fig. 12 Influence of volumetric steel ratio and web brace configuration at low axial load ratio

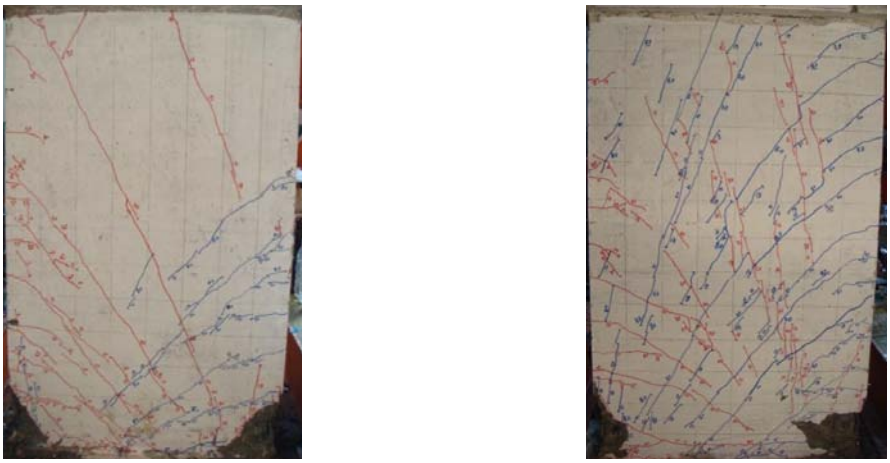

(a) CTSRC-6, ρ_{vb} = 0.25% (b) CTSRC-7, ρ_{vb} = 0.50%

Fig. 13 Influence of volumetric steel ratio of web brace under high axial load ratio of 0.25

5.2 Lateral load-displacement relationship

The measured lateral force versus lateral displacement hysteretic curves of all specimens are shown in Fig. 14. The hysteretic curves of all the specimens exhibited insignificant pinching phenomena. However, various hysteresis characteristics can be clearly seen due to the influence of the test parameters. The hysteretic curves of the specimens CTSRC-2 (Fig. 14(b)), CTSRC-3 (Fig. 14(c)) and CTSRC-4 (Fig. 14(d)) were fuller than CTSRC-1 (Fig. 14(a)), where web braces were not provided, indicating the positive influence of web brace on energy dissipation capacity. In addition, the hysteretic loops of specimen CTSRC-2 were better than specimens CTSRC-3 and CTSRC-4, where latticed batten plates were used as web braces instead of steel angles, showing that steel angles were more suitable to be used for web braces. Based on the comparison between

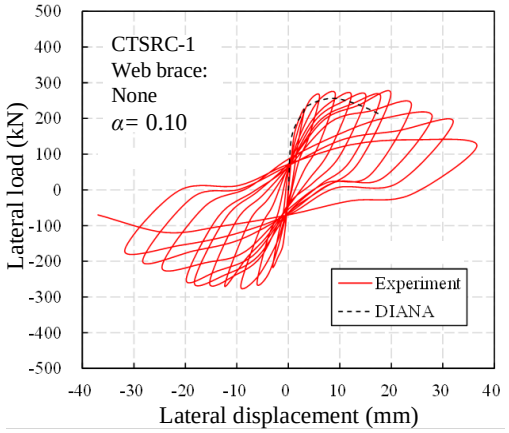

(a) Specimen CTSRC-1

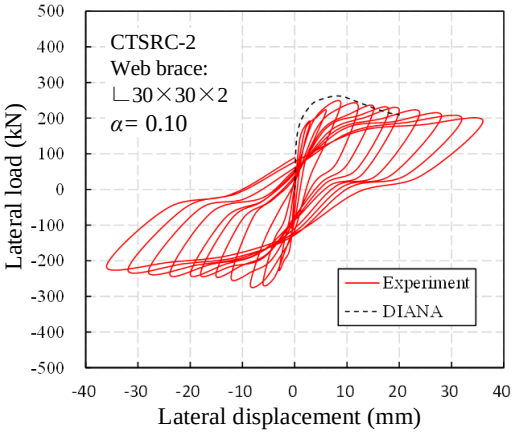

(b) Specimen CTSRC-2

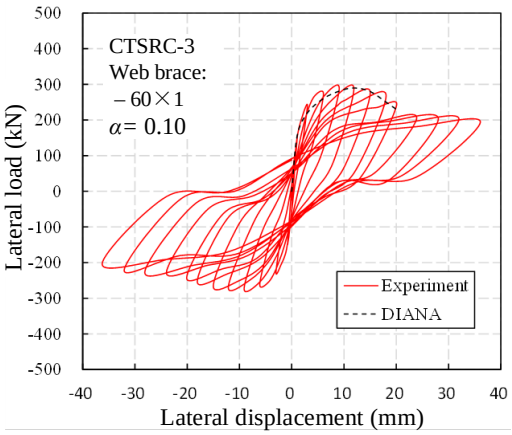

(c) Specimen CTSRC-3

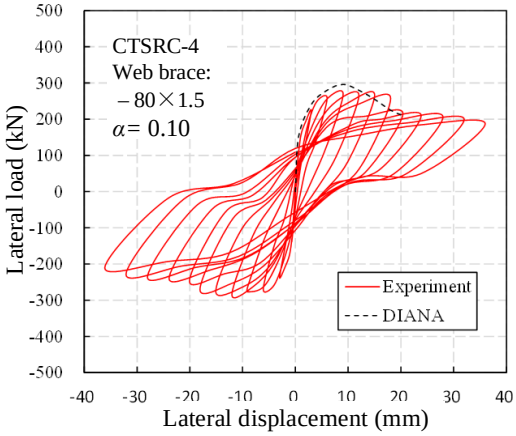

(d) Specimen CTSRC-4

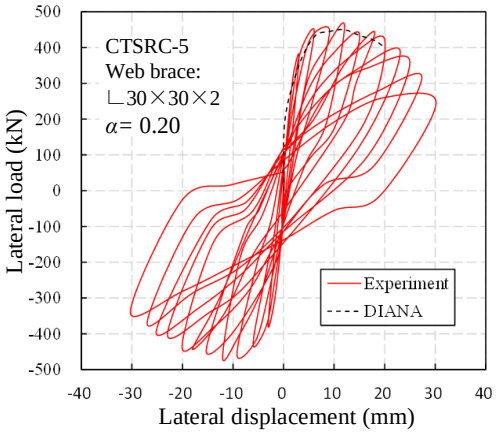

(e) Specimen CTSRC-5

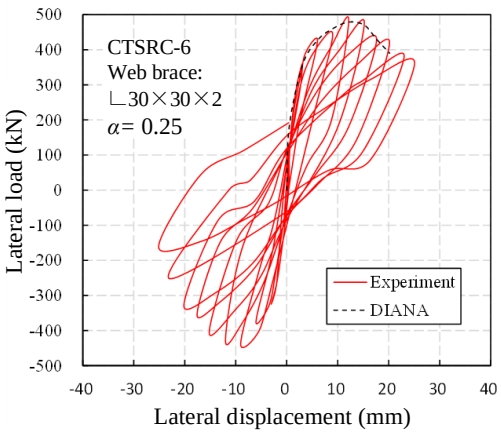

(f) Specimen CTSRC-6

Fig. 14 Measured lateral load-displacement responses of specimens

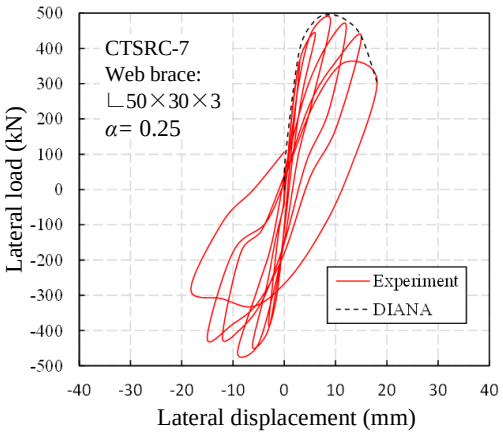

(g) Specimen CTSRC-7

Fig. 14 Continued

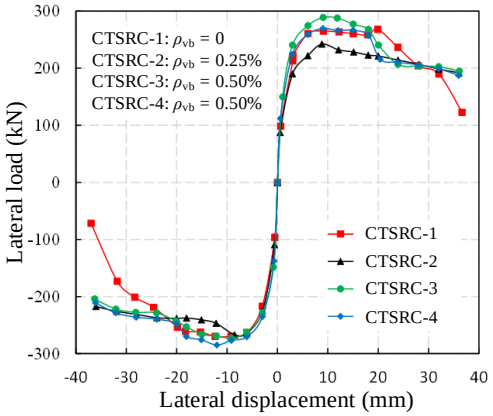

Fig. 15 Influence of ρ_{vb} when α = 1

specimens CTSRC-3 and CTSRC-4, the influence of volumetric steel ratio of web braces on the hysteretic loops was not significant. Specimens CTSRC-5 (Fig. 14(e)), CTSRC-6 (Fig. 14(f)) and CTSRC-7 (Fig. 14(g)) were subjected to relatively higher level of axial loads, resulting in narrower hysteretic curves than those specimens under low axial load ratios.

The measured lateral force-displacement skeleton curves of all specimens were shown and compared in Figs. 15-17 to examine the influences of test parameters on the initial stiffness, maximum lateral load capacity, post-yielding strength degradation characteristics. In Fig. 15, specimens CTSRC-1 to CTSRC-4 were compared in that they possessed various ρ_{vb} when α = 0.1. It can be seen that high volumetric steel ratio can generally increase the initial stiffness and maximum lateral load capacity. The post-yielding strength degradation trends were similar.

The skeleton curves of specimens CTSRC-2, CTSRC-5 and CTSRC-6 were compared in Fig. 16 to demonstrate the influence of axial load ratio. The higher the axial load ratio is, the higher initial stiffness and maximum lateral capacity are. However, the post-yielding behavior is significantly worsened for specimens with high axial load ratios. As a result, specimen CTSRC-2

exhibited the most stable and gradual strength degradation after the maximum load capacity has been reached.

Specimens CTSRC-6 and CTSRC-7 had various ρ_{vb} under a high level of axial load ratio. According to the comparison in Fig. 17, the volumetric steel ratio of web braces still doesn't have noticeable influence on the initial stiffness and maximum lateral load capacity.

5.3 Characteristic strengths and displacements

In order to estimate the displacement ductility of each specimen, the equivalent energy method proposed by Park 1988 was adopted to determine the yield displacement based on the skeleton curve of each specimen. As shown in Fig. 18, P_m and Δ_m are the maximum lateral force and the corresponding displacement on the skeleton curve; the ultimate condition is defined as the point on the skeleton curve where the shear force is equal to $0.85P_m$ and the corresponding displacement Δ_u is regarded as the maximum displacement. An idealized bilinear curve consisting of an ascending segment and a flat segment corresponding to the maximum shear force P_m is developed in the way

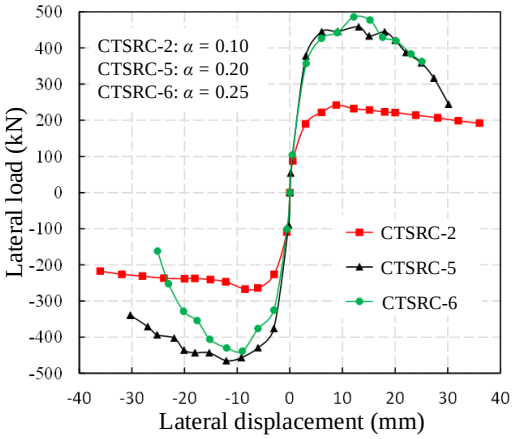

Fig. 16 Influence of α

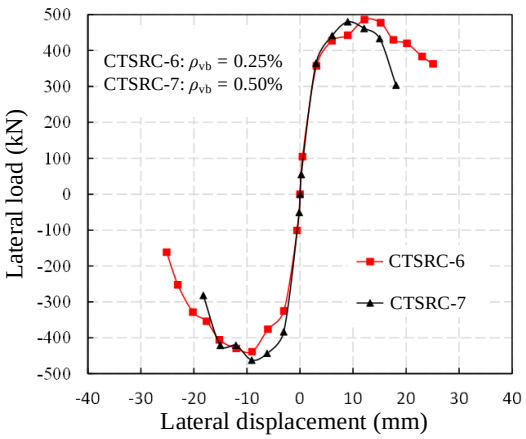

Fig. 17 Influence of ρ_{vb} when α =0.25

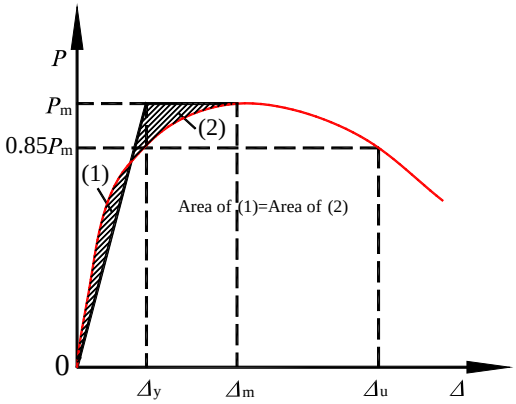

Fig. 18 Energy equivalence method

Table 3 Main test results

ID	Direc-tion	Initial cracking	Element yielding			Peak load			Failure		
		P_{cr} / kN	P_y / kN	Δ_y / mm	Δ_y/h_w	P_m / kN	Δ_m / mm	Δ_m/h_w	P_u / kN	Δ_u / mm	Δ_u/h_w
CTSRC-1	+	100	222.1	3.32	1/434	266.6	9.12	1/158	225.2	25.3	1/57
	-	100	225.5	3.31	1/435	269.6	9.23	1/156	229.2	23.16	1/62
CTSRC -2	+	90	207.2	3.04	1/474	242.2	8.81	1/163	205.9	28.48	1/51
	-	110	226.4	2.61	1/552	267.0	8.51	1/169	226.9	31.12	1/46
CTSRC -3	+	150	246.4	2.57	1/560	288.9	9.08	1/159	245.6	19.69	1/73
	-	150	228.9	2.46	1/585	272.6	9.12	1/158	231.7	23.10	1/62
CTSRC -4	+	110	232.1	2.38	1/605	269.6	9.04	1/159	229.2	19.62	1/73
	-	140	239.9	2.35	1/613	284.8	12.03	1/120	242.0	22.71	1/63
CTSRC -5	+	280	394.5	4.07	1/354	458.7	12.05	1/120	389.9	21.94	1/66
	-	300	392.6	4.28	1/336	465.1	12.07	1/119	395.3	24.53	1/59
CTSRC -6	+	240	409.8	4.71	1/306	485.8	12.14	1/119	412.9	20.53	1/70
	-	220	374.2	4.40	1/327	438.6	9.05	1/159	372.8	16.1	1/89
CTSRC -7	+	280	410.3	3.94	1/365	482.0	9.02	1/160	409.7	15.59	1/92
	-	300	393.8	3.54	1/407	465.8	9.11	1/158	392.6	15.70	1/92

illustrated in Fig. 18. If the shaded regions (1) and (2), enclosed by the measured skeleton curve and the ascending segment of the idealized bilinear curve, have the same area, the displacement corresponding to the intersecting point between the ascending and flat segments of the idealized bilinear curve is taken as the yield displacement Δ_y. The lateral loads and displacements corresponding to initial cracking, yielding, peak lateral load and failure of the all specimens are listed in Table 3. The ratios of the maximum strength P_m in the positive direction to negative direction for each specimen were between 0.91 and 1.11. The drift ratios corresponding to the

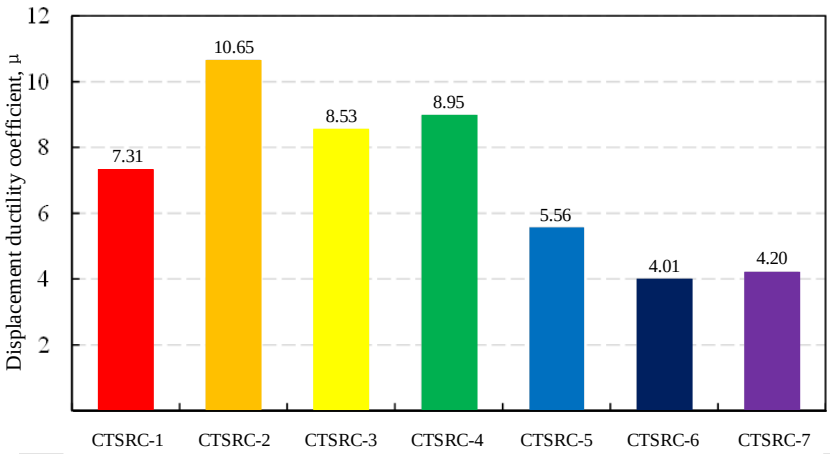

Fig. 19 Ductility coefficients of specimens

yielding were between 1/613 and 1/306 with an average value of 1/429. The ultimate drift ratios were 1/92 and 1/46 with an average of 1/66, which demonstrated the high deformation capacity of the specimens.

The ductility of the specimens was evaluated by the displacement ductility coefficient μ, which is calculated by $\mu = \Delta_u/\Delta_y$, where Δ_y and Δ_u are the lateral displacements at yielding and failure respectively. The value of the ductility coefficient μ for each test specimen is shown in Fig. 19. Evidently, the displacement ductility coefficient of CTSRC-2 is larger than that of CTSRC-1 by about 45.7%, indicating the displacement ductility can be significantly improved with encased truss web braces. The displacement ductility coefficients of CTSRC-3 and CTSRC-4 are 8.53 and 8.95, which were about 19.9 and 16.0% less than those of specimen CTSRC-2, respectively, implying that steel angles can be more effective in improving the displacement ductility coefficients than the latticed batten plates. With the same web brace configuration and the volumetric ratio of web brace, the increase of axial load ratio can lead to reduced displacement ductility.

5.4 Secant stiffness degradation

The stiffness degradation characteristics of specimens were evaluated by the secant stiffness corresponding to the maximum lateral load during the first cycle of each loading level. The initial stiffness, peak stiffness and ultimate stiffness are illustrated in Table 4. Clearly, the initial stiffness of specimens CTSRC-5, CTSRC-6 and CTSRC-7 are much higher than CTSRC-1, CTSRC-2, CTSRC-3 and CTSRC-4, and similar tendency of the peak stiffness and ultimate stiffness can be noticed. As shown in Figs. 20(a)-(g), the stiffness degradation characteristics in the positive and negative directions are very similar for each specimen. The process of stiffness degradation is almost the same for all specimens, indicating that the key parameters have little effect on the stiffness degradation characteristics.

Table 4 Characteristic point stiffness of specimens

ID	Direction	Initial stiffness (kN/mm)	Peak stiffness (kN/mm)	Ultimate stiffness (kN/mm)
CTSRC-1	+	153.5	29.0	9.1
	-	177.1	29.2	9.9
CTSRC -2	+	163.2	27.5	7.2
	-	190.1	31.4	7.3
CTSRC -3	+	144.9	31.8	12.3
	-	184.3	29.9	10.0
CTSRC -4	+	194.7	29.8	11.7
	-	199.6	23.7	10.7
CTSRC -5	+	186.3	38.1	17.6
	-	218.7	38.5	18.3
CTSRC -6	+	224.2	40.0	16.6
	-	183.3	48.5	16.3
CTSRC -7	+	216.1	53.3	16.8
	-	192.7	50.7	15.5

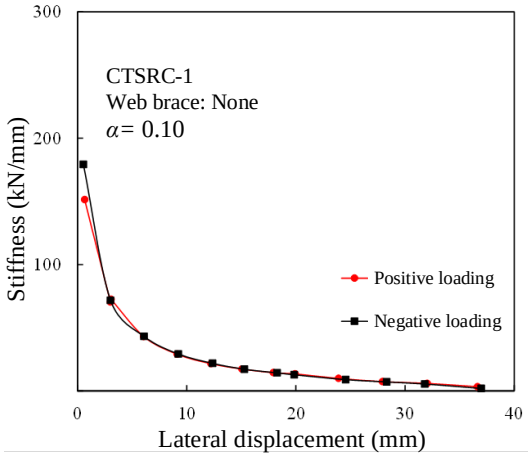

(a)

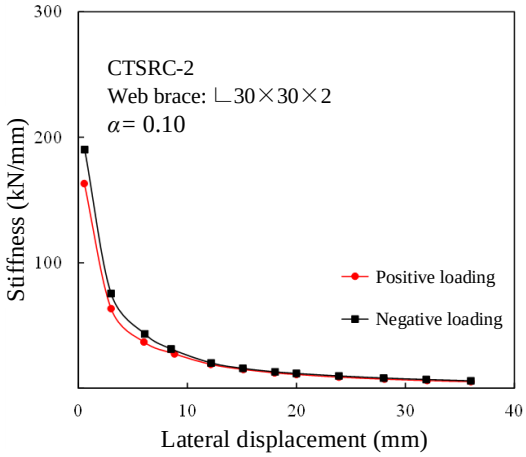

(b)

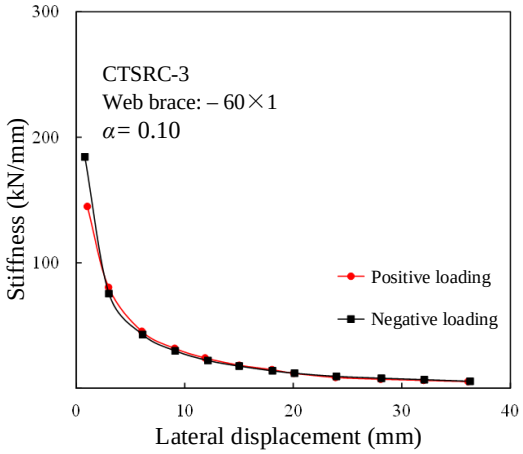

(c)

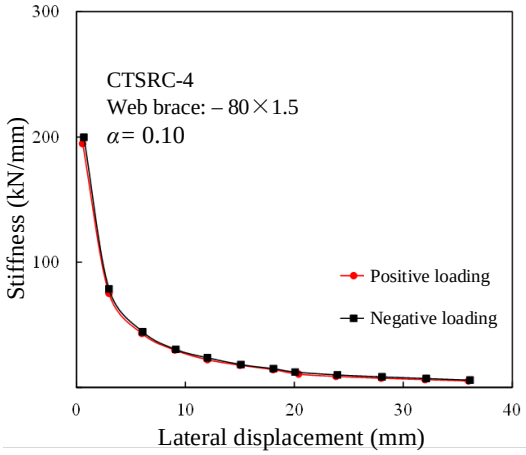

(d)

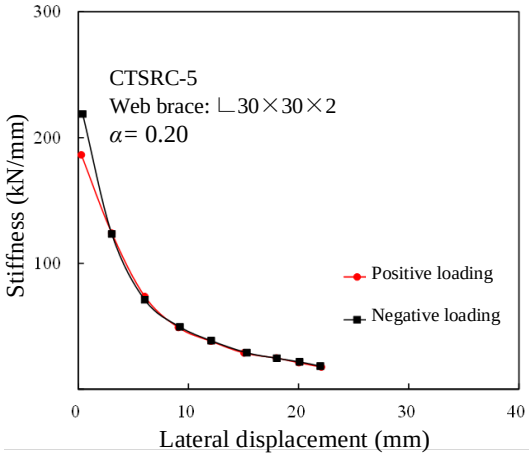

(e)

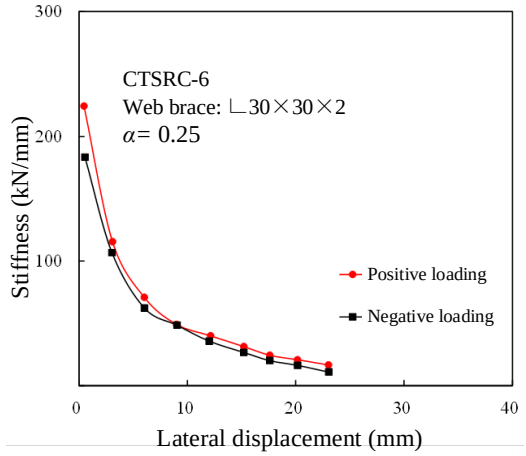

(f)

Fig. 20 Stiffness degradation curves

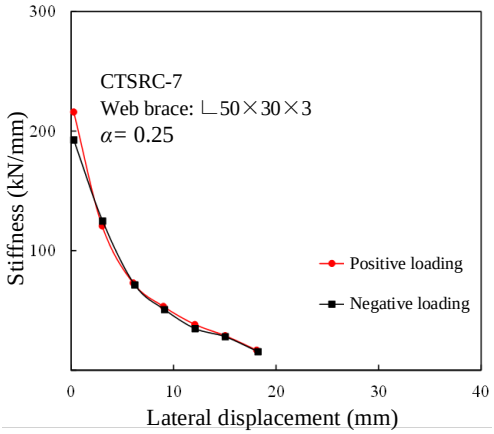

(g)

Fig. 20 Continued

5.5 Energy dissipation capacity

The energy dissipation in each cycle of loading was evaluated by the area enclosed by the hysteretic loop of one cycle from the horizontal load versus lateral displacement hysteretic curves. A comparison between the total energy dissipation of each specimen is presented in Fig. 21. Clearly, the energy dissipation of CTSRC-2 is larger than that of CTSRC-1 by about 40%, showing that the energy dissipation can be significantly improved with encased web braces. The energy dissipation of CTSRC-3 and -4 are 26.25 and 27.97 kJ, which are about 17.6 and 12.2% less than that of specimen CTSRC-2, respectively, implying that the steel angle is more effective than the latticed batten plates in enhancing the energy dissipation capacity. With the same configuration and volumetric ratio of web braces, the higher axial load ratio can result in decreased energy dissipation capacity.

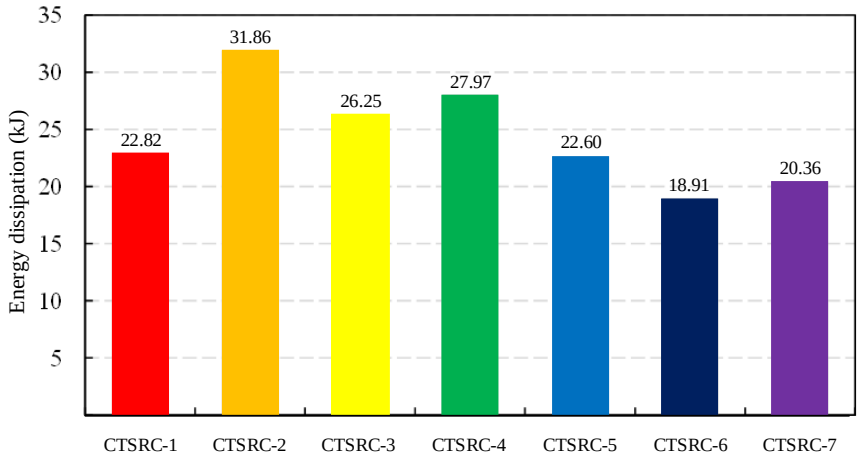

Fig. 21 Total energy dissipation of specimens

Table 5 Comparison of predicted and tested maximum load capacity (kN)

Specimen	V_u by test	V_u^d by DIANA	V_u^c by JGJ138-2012	V_u / V_u^d	V_u / V_u^c
CTSRC-1	267	256	228	1.04	1.17
CTSRC-2	242	262	248	0.92	0.98
CTSRC-3	289	281	245	1.03	1.18
CTSRC-4	270	296	250	0.91	1.08
CTSRC-5	459	450	408	1.02	1.13
CTSRC-6	486	479	421	1.01	1.15
CTSRC-7	482	496	433	0.97	1.11

5.6 Comparison of predicted and tested results

The backbone curves (dashed lines) obtained from the numerical finite element analysis using DIANA were plotted together with the lateral load-displacement hysteretic loops (solid lines) in Fig. 14. It is obvious that the numerically predicted backbone curves had a very good agreement with the tested ones in terms of initial stiffness and post-yielding load-displacement relationship. The suggested modeling techniques can be used to analyze the overall seismic behavior of composite walls with encased CFTW steel truss.

Table 5 shows the maximum load-carrying capacities of the wall specimens obtained by tests, DIANA and JGJ138-2012 (2012). It can be seen the test results agree well with the predicted results.

6. Conclusions

In this research program, the RC walls with encased CFTW steel truss that are more suitable to be used in ordinary high-rise buildings located in regions of high seismicity than conventional RC walls and SRC walls are proposed and studied. The seismic performance of seven scaled wall specimens was evaluated in terms of the maximum lateral load carrying capacity, post-yielding deformation and energy dissipation capacities, and strength and stiffness degradation characteristics. Based on the results and discussions, the following conclusions can be drawn.

- The existence of web brace can introduce more lateral force to be resisted by the wall web region, resulting in more inclined cracks developed at web region of the wall. The further increase of volumetric steel ratio of web brace cannot significantly change the cracking and failure pattern of the wall.
- The steel angle is a more suitable web brace configuration than the latticed batten plates in terms of ensuring the displacement ductility and energy dissipation.
- The volumetric steel ratio of encased web brace has little influence on the displacement ductility, energy dissipation and lateral load capacity. So it is not effective to increase the steel ratio for better seismic behavior of the composite wall.
- Higher axial load ratios can increase the lateral load capacity of walls, but result in reduced displacement ductility and energy dissipation capacity.
- The suggested finite element modeling techniques can be used to accurately predict the backbone curves of composite walls with encased CFTW steel truss.

- The calculation method provided in the Chinese Code for Design of Composite Structures (JGJ138-2012 2012) can accurately predict the maximum lateral load capacity of composite walls with encased CFTW steel truss.
- From the perspective of seismic design, optimum design can be achieved according to the experimental results. Particularly, the steel angle is the preferred type of the encased web brace. The volumetric steel ratio of 0.25% of encased web brace is a cost-effective value in ensuring satisfactory energy dissipation capacity and displacement ductility. In order to avoid the adverse effect on the ductility behavior, the axial load ratio should be limited to the maximum level, about 0.20 for the nominal value or about 0.50 for the design value.

Acknowledgments

This research project is financially sponsored by the National Science Foundation of China under the grant number of 51578090 and the grant by Chongqing Science and Technology Commission under the contract number of CSTC2015JCYJYS0004. The authors would like to express their sincere thanks and appreciation to various supporting agencies of this project.

References

Cao, W.L., Zhang, J.W., Dong, H.Y. and Deng, T.L. (2009), "Seismic performance of high-rise shear wall with concealed truss", *J. Harbin Inst. Technol.*, **41**(4), 153-158.

China Ministry of Construction (2003), GB500017-2003, Code for design of steel structures, Beijing, China.

China Ministry of Construction (2010), GB500010-2010, Code for design of concrete structures, Beijing, China.

China Ministry of Construction (2011), GB500010-2011, Code for seismic design of buildings, Beijing, China.

China Ministry of Construction (2012), JGJ138-2012, Code for design of composite structures, Beijing, China.

Dan, D., Fabian A. and Stoian, V. (2011), "Theoretical and experimental study on composite steel–concrete shear wall with vertical steel encased profiles", *J. Constr. Steel Res.*, **67**(5SI), 800-813.

Dazio, A., Beyer, K. and Bachmann, H. (2009), "Quasi-static cyclic tests and plastic hinge analysis of RC structural walls", *Eng. Struct.*, **31**(7), 1556-1571.

DIANA Version 9.4.4 (2012), Finite element analysis user's manual-nonlinear analysis; TNO Building and Construction Research, Delft, the Netherlands.

Eom, T.S., Park, H.G., Lee, C.H., Kim, J.H. and Chang, I.H. (2009), "Behavior of double skin composite wall subjected to in-plane cyclic loading", *J. Struct. Eng.*, **135**(10), 1239-1249.

Feenstra, P.H. (1993), "Computational aspects of biaxial stress in plain and reinforced concrete", Ph.D. Thesis; Delft University of Technology, Delft, The Netherlands.

Hines, E.M., Seible, F. and Priestley, M.J.N. (2002), "Cyclic tests of structural walls with highly-confined boundary elements", Report No. SSRP-2001/27; University of California, San Diego, CA, USA.

Nie, J.G., Hu, H.S., Fan, J.S., Tao, M.X., Li, S.Y. and Liu, F.J. (2013), "Experimental study on seismic behavior of high strength concrete filled double-steel-plate composite walls", *J. Constr. Steel Res.*, **88**(9), 206-219.

Park, R. (1988), "Ductility evaluation from laboratory and analytical testing", *Proceedings of the 9th World Conference on Earthquake Engineering*, Tokyo-Kyoto, Japan, August, pp. 605-616.

Rafiei, S., Hossain, K.M.A., Lachemi, M. and Behdinan, K. (2015), "Composite wall with high performance concrete subjected to monotonic shear", *J. Constr. Steel Res.*, **107**, 124-136.

Sayre, B. (2003), "Performance evaluation of steel reinforced shear walls", Thesis for the degree of Master

of Science; University of California, Los Angeles, CA, USA.
Thomas, T. (1993), CEB-FIP Model Code-1990; CEB Bulletin No. 213-214, Lausanne, Switzerland.
Thomsen, J.H. and Wallace, J.W. (2004), "Displacement-based design procedures for slender reinforced concrete structural walls-experimental verification", *J. Struct. Eng*., **130**(4), 618-630.
Vallenas, J.M., Bertero, V.V. and Popov, E.P. (1979), "Hysteretic behaviour of reinforced concrete structural walls", Report No. UBC/EERC-79/20; University of California, Berkeley, CA, USA.
Zhao, Q.H. and Astaneh-Asl, A. (2004), "Cyclic behavior of traditional and innovative composite shear walls", *J. Struct. Eng*., **130**(2), 271-284.

BU

Nomenclature

The following symbols are used in this paper:

h_w	height of shear wall
l_w	width of shear wall
α	axial load ratio
ρ_{vb}	volumetric ratio of the encased truss web braces
$\varepsilon_{c/3}$	strain at which one-third of the maximum compressive strength is reached
ε_c	strain at which the maximum compressive strength is reached
ε_u	ultimate strain at which the material is completely softened in compression
f_c	compressive strength of concrete
f_t	tensile strength of concrete
E	young's modulus
G_C	total compressive fracture energy
G_F	total tensile fracture energy
h	characteristic element length
$\tau_{\max}$	bond strength
τ_f	residual bond stress
S	relative slip between steel and concrete
B	empirical coefficient
V_u	maximum lateral load capacity of experiment
V_u^d	predicted maximum lateral load by DIANA
V_n^c	predicted maximum lateral load by JGJ138-2012
M	bending moment at wall section
V	shear force at wall section
λ	shear span ratio
f_c	compressive strength of concrete
b_w	thickness of the shear wall
h_{w0}	effective depth of shear wall
N	axial force
A_w	web area of shear wall
A	area of shear wall
f_{yv}	design tensile of horizontal distribution reinforcement
S	vertical distance of horizontal distribution reinforcement
A_{sh}	total area of the horizontal distribution reinforcement on the same section of shear wall

f_a	design tensile of shape steel on the edge of the shear wall
A_a	area of shape steel on the tensile edge of the shear wall
f_g, f'_g	design tensile and compressive of steel diagonal bracing
A_g, A'_g	tensile and compressive area of steel diagonal bracing
φ	stability coefficient of web brace in compression
α	angle between the web brace and horizontal plane
u	displacement ductility coefficient
P_m	maximum lateral load
Δ_m	corresponding lateral displacement for the maximum lateral load
P_u	ultimate lateral load
Δ_u	ultimate lateral displacement
P_y	yield lateral load
Δ_y	lateral displacement at yield